Effect of Large-Scale Circulation Anomalies on Summer Rainfall over the Yangtze River Basin: Tropical versus Extratropical

Xinyu Li,[a,b] Riyu Lu,[c,d] and Xidong Wang[a,b]

[a] *Key Laboratory of Marine Hazards Forecasting, Ministry of Natural Resources, Hohai University, Nanjing, China*
[b] *College of Oceanography, Hohai University, Nanjing, China*
[c] *State Key Laboratory of Numerical Modeling for Atmospheric Sciences and Geophysical Fluid Dynamics, Institute of Atmospheric Physics, Chinese Academy of Sciences, Beijing, China*
[d] *College of Earth and Planetary Sciences, University of the Chinese Academy of Sciences, Beijing, China*

ABSTRACT: This study investigates the tropical and extratropical circulation anomalies that directly affect the summer rainfall over the Yangtze River basin (YRB). In the lower troposphere, the tropical circulation anomalies that enhance the YRB rainfall manifest as an anticyclonic anomaly over the tropical western North Pacific (WNP) and the extratropical circulation anomalies are characterized by northeasterly anomalies to the north of the YRB. It is found that the heavier the YRB rainfall, the more necessary the cooperation between the tropical WNP anticyclonic anomaly and the midlatitude northeasterly anomalies, and compared to the tropical WNP anticyclonic anomaly, the midlatitude northeasterly anomalies can more efficiently induce the YRB rainfall. Further results indicate that the tropical WNP anticyclonic anomaly exhibits notable quasi-biweekly feature and provides a favorable background for the enhanced YRB rainfall. By contrast, the northeasterly anomalies are dominated by synoptic variability. Furthermore, there are significant precursor signals for the lower-tropospheric northeasterly anomalies. These signals manifest as the eastward propagation of two wave trains in the upper troposphere: a midlatitude one and a high-latitude one, which tend to be independent. The midlatitude one originates around the Mediterranean Sea and propagates eastward along the Asian westerly jet. The high-latitude one propagates over the high-latitude Eurasian continent, from Europe eastward to Lake Baikal and then southeastward to East Asia.

KEYWORDS: Atmospheric circulation; Rainfall; Anomalies

1. Introduction

The Yangtze River basin (YRB) is the most densely populated region in China, but has been subject to heavy floods throughout history (Plate 2002; Yu et al. 2009). For example, the devastating flood in 1998 caused more than 3000 deaths, 250 billion yuan (RMB; US$40 billion) in direct economic loss and made 15 million people homeless (Lu 2000). Therefore, summer rainfall variabilities over the YRB have been an important research subject for many decades (e.g., Tao and Chen 1987; Ding 1992; Mao et al. 2010; Liu et al. 2014; Li and Lu 2017, 2021; Li et al. 2020; Ding et al. 2021).

Located in the subtropical area of eastern China, the YRB is simultaneously affected by the tropical and extratropical large-scale systems during summer months (Tao and Chen 1987; Ding 1992, 2005; Zhu et al. 2007; Chen and Zhai 2015). The tropical southwesterly flows from warm oceans meet northerly or northeasterly cold air from middle and high latitudes over the YRB, forming the so-called mei-yu front (Ding 1992; Zhu et al. 2007; Ninomiya and Shibagaki 2007). The mei-yu front is characterized by weak temperature gradients but high equivalent potential temperature gradients due to the strong meridional moisture contrast (Chen and Chang 1980; Ding 1992, 2005; Zhu et al. 2007; Sampe and Xie 2010; Chen and Zhai 2015; Li and Lu 2017). The mei-yu front is a result of the tropical–extratropical contrast and acts as the most important factor that causes the YRB rainfall in summer. Therefore, tropical and extratropical circulation anomalies are both crucial for the YRB rainfall anomalies.

The most important factor that dominates the tropical southwesterly anomalies is the zonal shift of the western North Pacific (WNP) subtropical high in the lower troposphere. The westward extension (eastward retreat) of the subtropical high corresponds to an anticyclonic (cyclonic) anomaly in the tropical WNP, and favors enhanced (suppressed) rainfall over the YRB through modifying the southwesterly water vapor transport (e.g., Huang and Sun 1992; Zhou and Yu 2005; Li and Lu 2017). The zonal shift of the subtropical high presents multiscale features, ranging from daily to biweekly and from intraseasonal to interannual time scales (Park et al. 2010; Mao et al. 2010; Yang et al. 2010; Ren et al. 2013; Xie et al. 2016; Ding et al. 2021). Substantial efforts have been made to explore the zonal shift of the subtropical high and the associated YRB rainfall on different time scales (e.g., Hsu and Weng 2001; Yang et al. 2010; Ren et al. 2013; Liu et al. 2014; Chen et al. 2015; Li et al. 2015, 2021). For example, some studies showed that the subseasonal zonal oscillation of the subtropical high is associated with the quasi-biweekly oscillation propagating northwestward from the tropical to subtropical WNP (Hsu and Weng 2001; Jia and Yang 2013; Chen et al. 2015; Li et al. 2015). Other studies reported that the 10–30- and 20–50-day oscillation of summer rainfall over the YRB are the response to the subtropical high
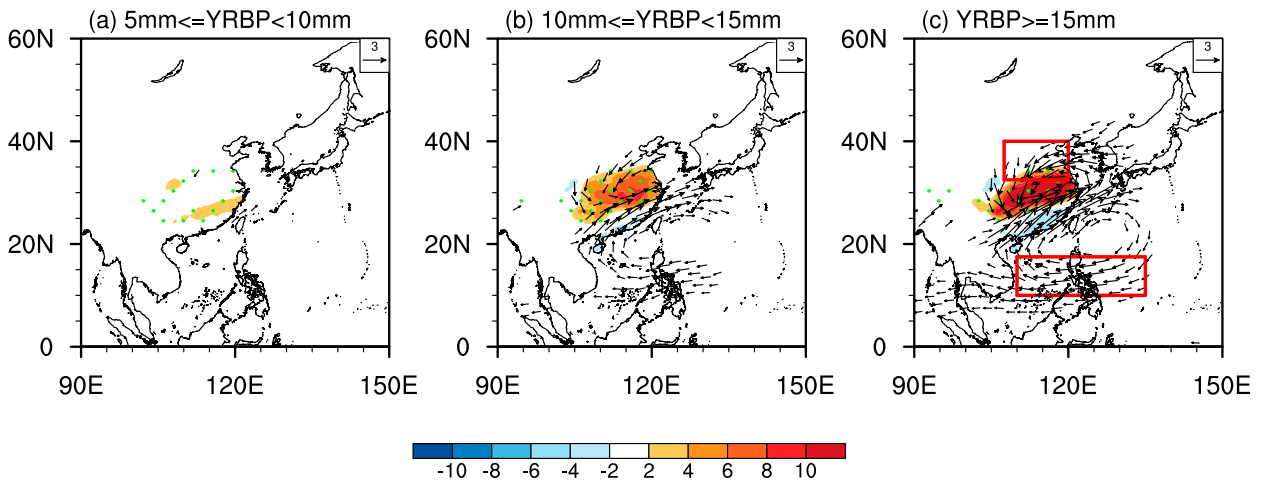

FIG. 1. Composite 850-hPa horizontal wind anomalies (vectors; m s^{-1}) and rainfall anomalies (shading; mm day^{-1}) associated with different YRBPI intensities: (a) $5 \leq$ YRBPI ≤ 10 mm day^{-1}, (b) $10 \leq$ YRBPI ≤ 15 mm day^{-1}, and (c) YRBPI ≥ 15 mm day^{-1}. Shading significant at the 95% confidence level is stippled as green and vectors are shown only when they are significant in at least one direction. The marked regions in (c) are used to define WNPUI and NEI (see text for details).

with the same time-scale variation (e.g., Liu et al. 2008; Mao et al. 2010; Ren et al. 2013).

There are diverse systems that play an important role in affecting the extratropical cold and dry air, including the blocking high (Zhu et al. 2007; Chen and Zhai 2015; Ding et al. 2021), the northeast cold vortex (He et al. 2007; Hu et al. 2011; Xu and Qi 2023), the upper-tropospheric westerly jet (Liang and Wang 1998; Wang et al. 2019), and the disturbances along the westerly waveguide (Sampe and Xie 2010; Liu et al. 2014). Most of the previous results revealing the roles of these extratropical systems in affecting the YRB rainfall are based on case study of extreme rainfall events and the extratropical circulation anomalies in the upper troposphere vary from case to case. The common features of the extratropical circulation anomalies, especially the precursor signals for the extratropical cold and dry air, appear to be deficient.

Based on case study or composite analysis, previous studies have widely explored the circulation anomalies from the perspective of extreme rainfall events (e.g., Ding 2005; Zhu et al. 2007; Chen and Zhai 2015; Ding et al. 2021). However, the individual characteristics of the tropical and extratropical circulation anomalies that affect the YRB rainfall are not fully understood. In this study, we aim to answer the following questions: How do the tropical and extratropical circulation anomalies vary with the intensity of YRB rainfall? Are tropical circulation anomalies or extratropical circulation anomalies more effective in causing the YRB rainfall? And is there any precursor signal for the tropical and extratropical circulation anomalies?

The rest of this paper is organized as follows. Section 2 describes the datasets and methods used in this study. Section 3 explores the tropical and extratropical circulation anomalies associated with the YRB rainfall. Section 4 investigates the evolutions of the tropical and extratropical circulation anomalies to detect the precursor signals. Section 5 is devoted to a summary and discussion.

2. Data, definitions, and methods

a. Data

This study uses the daily mean reanalysis data from the fifth generation European Centre for Medium–Range Weather Forecast (ECMWF) reanalysis (ERA5; Hersbach et al. 2020), including horizontal wind, specific humidity, and air temperature. Also used are the daily gridded observational precipitation data from the National Climate Center of China (version of CN05.1; Wu and Gao 2013). The horizontal resolution is $0.5° \times 0.5°$ for the ERA5 and $0.25° \times 0.25°$ for the CN05.1. The current analysis covers the period from 1979 to 2020 and the months of June–August are used to represent summer.

b. Definitions

We define three indices to facilitate the descriptions of YRB rainfall and tropical and extratropical circulation anomalies in the lower troposphere. The YRB is defined as the land area in mainland China east of 107.5°E and between 27° and 34°N, which is identical to the location used in earlier studies (Chang et al. 2000; Li and Lu 2017, 2018). The Yangtze River basin precipitation index (YRBPI) is defined as the precipitation averaged over the defined YRB. We use a WNP zonal wind index (WNPUI) to describe the tropical circulation anomalies that affect the YRB rainfall. The WNPUI is defined as the 850-hPa zonal wind anomalies averaged over 10°–17.5°N, 110°–135°E, and then multiplied by -1. The zonal wind anomalies over this region are most associated with the YRB rainfall in the tropics (Fig. 1c). A positive (negative) WNPUI tends to correspond to an anticyclonic (cyclonic) anomaly over the tropical WNP. The northeasterly index (NEI) is defined as the northeasterly anomalies averaged over 32.5°–40°N, 107.5°–120°E, following Li and Lu (2018). The northeasterly anomalies over this region directly affect the YRB rainfall from the extratropics (Fig. 1c). The NEI can be written as
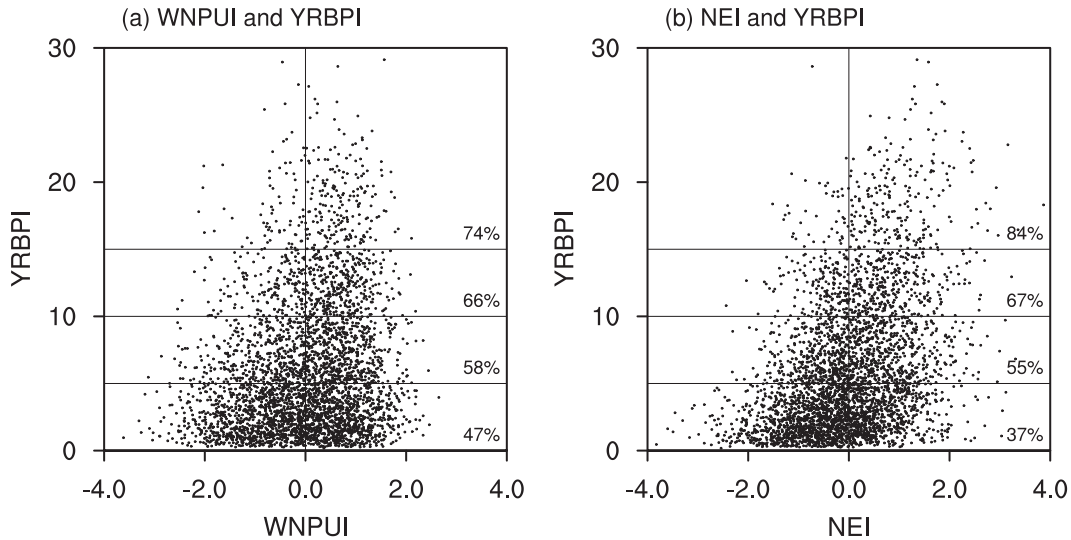
FIG. 2. Scatter diagrams of the original YRBPI and the standardized (a) WNPUI and (b) NEI. Horizontal lines indicate that the YRBPI equals 5, 10, and 15 mm day^{-1}, respectively. The proportion of positive YRBPI cases for each category of YRBPI intensity is marked correspondingly.

$$NEI = A_{ave}[u\cos(-135°) + v\sin(-135°)].$$

Here, A_{ave} represents the area average, and u and v are the 850-hPa zonal and meridional wind anomalies, respectively. A positive (negative) NEI indicates northeasterly (southwesterly) anomalies to the north of the YRB. In this study, daily anomalies are obtained by deducting the climatology of that particular day from the raw data.

c. Methods

The composite analysis is mainly used in this study. We use the two-tailed Student's t test to evaluate the significance of each variable at each grid point (Wilks 2006). The effective sample size N^* at each grid point is computed by $N^* = N \times (1 - r_1)/(1 + r_1)$, where N refers to the original length of the time series and r_1 is the lag-1 autocorrelation coefficient (Zwiers and von Storch 1995).

3. Tropical and extratropical circulation anomalies associated with the YRB rainfall in summer

Figure 1 shows the composite rainfall and 850-hPa horizontal wind anomalies associated with different intensities of the YRB rainfall. We roughly classify the cases with YRBPI greater than 5 mm day^{-1}, which is near to the average of YRBPI during the analyzed period, into three categories: $5 \leq$ YRBPI ≤ 10 mm day^{-1}, $10 \leq$ YRBPI ≤ 15 mm day^{-1} and YRBPI ≥ 15 mm day^{-1}. There are 1033 cases for $5 \leq$ YRBPI $\leq$ 10 mm day^{-1}, 516 cases for $10 \leq$ YRBPI ≤ 15 mm day^{-1}, and 273 cases for YRBPI ≥ 15 mm day^{-1}, respectively. In summer, 5, 10, and 15 mm day^{-1} are the 53%, 80%, and 93% quantiles of the YRB rainfall, respectively, and thus the category YRBPI $\geq$ 15 mm day^{-1} is attributed to extreme rainfall over the YRB. Note that the results are not sensitive to the classification criteria,

for instance, by analyzing the categories of $6 \leq$ YRBPI $\leq$ 12 mm day^{-1}, $12 \leq$ YRBPI ≤ 18 mm day^{-1}, and YRBPI $\geq$ 18 mm day^{-1} could obtain similar results.

For all categories (Figs. 1a–c), there are positive rainfall anomalies over the YRB, and the lower-tropospheric circulation anomalies are characterized by an anticyclonic anomaly over the tropical WNP and a shear line-like cyclonic anomaly over the YRB, consistent with a number of previous studies (e.g., Yang et al. 2010; Ding et al. 2014, 2015; Hu et al. 2019; Cheng et al. 2021). Significant easterly anomalies appear over the south flank of the tropical WNP anticyclonic anomaly and northeasterly anomalies act as a major part of the midlatitude cyclonic anomaly. There are southwesterly anomalies between the tropical anticyclonic anomaly and the midlatitude cyclonic anomaly. Note that these southwesterly anomalies are associated with both the tropical anticyclonic anomaly and the midlatitude cyclonic anomaly and thus we use the tropical easterly anomalies (WNPUI) and midlatitude northeasterly anomalies (NEI) to represent tropical and extratropical circulation anomalies in the lower troposphere, respectively, as illustrated in section 2.

It is clear that associated with the increase of the YRB rainfall, both tropical and midlatitude circulation anomalies become stronger and more significant (Figs. 1a–c). The WNPUI (NEI) is 0.34 (0.39), 1.16 (0.94), and 1.68 (1.82) m s^{-1} for $5 \leq$ YRBPI ≤ 10 mm day^{-1}, $10 \leq$ YRBPI ≤ 15 mm day^{-1}, and YRBPI ≥ 15 mm day^{-1}, respectively. These results suggest that the heavier the YRB rainfall, the more necessary it is for the joint effect of the tropical and midlatitude circulation anomalies.

Figure 2 shows the scatter diagrams of the YRBPI and standardized WNPUI and NEI. The proportions of the positive WNPUI and NEI cases both increase with the YRBPI, confirming that the tropical and midlatitude circulation anomalies
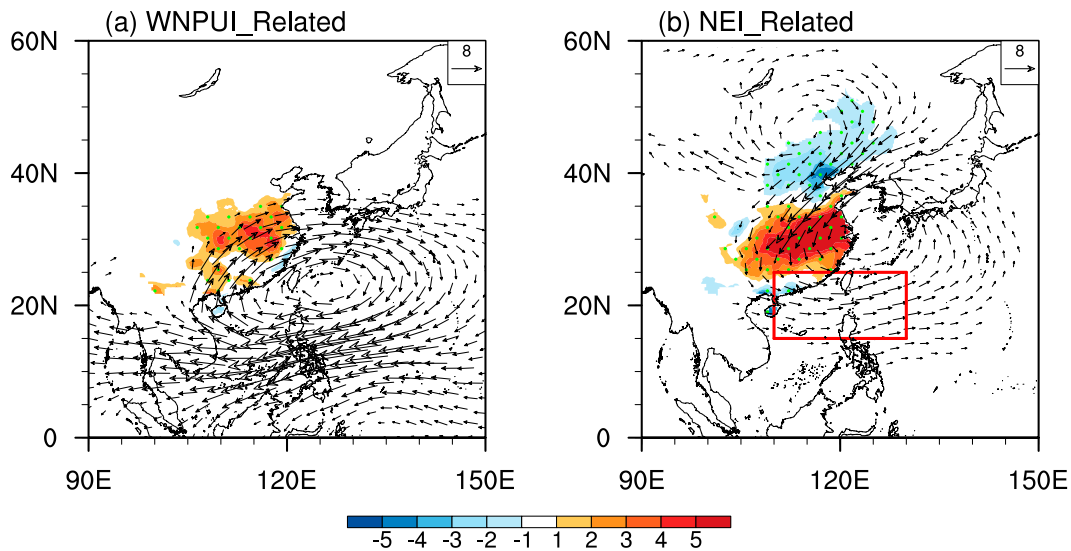
UV850 and Rainfall

FIG. 3. Composite 850-hPa horizontal wind anomalies (vectors; m s^{-1}) and rainfall anomalies (shading; mm day^{-1}) associated with (a) WNPUI and (b) NEI. Shading significant at the 95% confidence level is stippled as green and vectors are shown only when they are significant in at least one direction. The marked region in (b) indicates the area where the zonal wind anomalies are significantly associated with the NEI, which are excluded in Fig. 6b.

both significantly affect the YRB rainfall. On the other hand, the proportion of positive NEI cases increases faster than the positive WNPUI cases. For instance, the proportion of positive WNPUI cases is 47% for YRBPI $\leq$ 5 mm day^{-1} and increases to 74% for YRBPI $\geq$ 15 mm day^{-1} (Fig. 2a), but for positive NEI cases, the proportion increases from 37% to 84% (Fig. 2b). These results imply that the mid-latitude circulation anomalies may exert a more significant influence on the YRB rainfall than the tropical circulation anomalies.

To explore the physical mechanisms connecting the tropical or midlatitude circulation anomalies and the YRB rainfall, we select the cases with the absolute values of WNPUI or NEI greater than 0.7 standard deviations and perform composite analyses based on these cases. Using other criteria, such as 1.0 or 1.5 standard deviations, could obtain similar results. There are 1035 WNPUI+ cases, 937 WNPUI− cases, 916 NEI+ cases, and 914 NEI− cases selected. It was found that the circulation and rainfall anomalies are basically antisymmetric between the WNPUI+ and WNPUI− cases, and also between the NEI+ and NEI− cases (not shown). Therefore, the composite difference between WNPUI+ and WNPUI− cases and that between the NEI+ and NEI− cases are used to represent the anomalies associated with WNPUI and NEI, respectively. In addition, we have also examined the anomalies by using regression analysis and obtained similar results (not shown), confirming that the results are reliable.

Figure 3 shows the 850-hPa horizontal wind anomalies and rainfall anomalies associated with WNPUI and NEI,

respectively. For WNPUI (Fig. 3a), the lower-tropospheric circulation anomalies are characterized by an anticyclonic anomaly over the tropical WNP. This anticyclonic anomaly enhances water vapor transport to East Asia (Huang and Sun 1992; Lu and Dong 2001; Zhou and Yu 2005; Li and Lu 2017, 2018) and significant positive rainfall anomalies appear over the YRB. For NEI (Fig. 3b), the lower-tropospheric circulation anomalies are featured with an anticyclonic anomaly over eastern Mongolia and northeast China and a cyclonic anomaly over the YRB and East China Sea, and between the anticyclonic and cyclonic anomalies are significant north-easterly anomalies. Associated with the cyclonic anomaly and anticyclonic anomaly, there are enhanced rainfall over the YRB and suppressed rainfall over North China and northeast China, respectively.

We note that the NEI-related circulation anomalies show significant westerly anomalies over the tropical WNP (Fig. 3b), suggesting that there is a connection between the tropical and midlatitude circulation anomalies. Figure 4a shows the scatter diagram of the standardized WNPUI and NEI. The WNPUI and NEI tend to be negatively connected, with a total of 2135 cases in the second and fourth quadrants and 1729 cases in the first and third quadrants. This negative WNPUI–NEI connection explains the cases with negative (positive) WNPUI or NEI but strong (weak) YRB rainfall shown in Fig. 2. For example, for the correspondence of negative WNPUI and positive YRBPI anomaly, there are northeasterly anomalies to the north of the YRB (not shown), which favor the enhanced YRB rainfall; and for the correspondence of negative NEI and positive YRBPI anomaly, an anticyclonic anomaly appears over the tropical
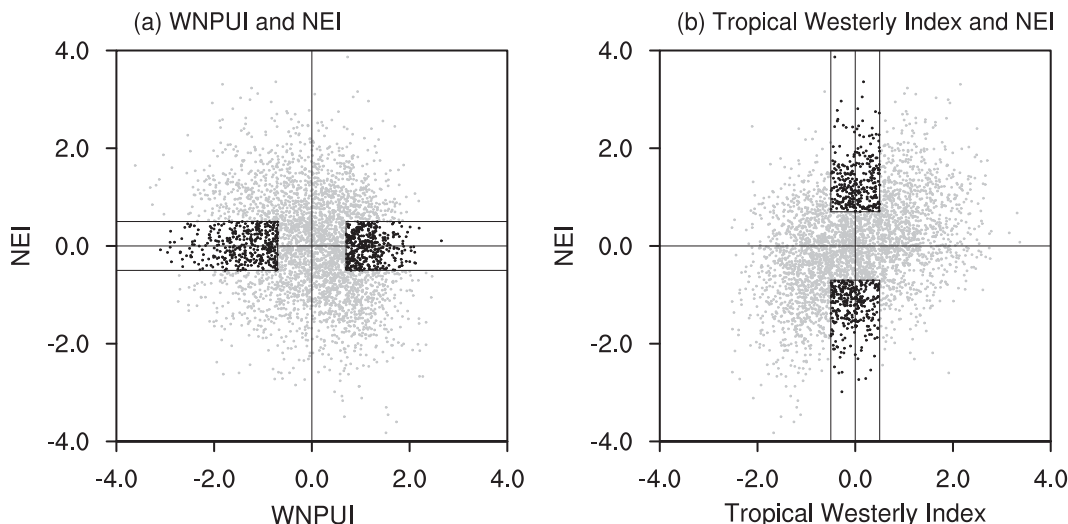
FIG. 4. Scatter diagrams of the standardized NEI and (a) WNPUI and (b) tropical westerly index (see text for definition). In (a), black dots in the rectangles indicate the cases with absolute values of WNPUI greater than 0.7 standard deviations and that of NEI smaller than 0.5 standard deviations, which are selected to remove the extratropical signal from WNPUI. Similarly, black dots in (b) are selected to remove the tropical signal from NEI. Note that NEI tends to be positively connected with the tropical westerly index, but negatively connected with WNPUI, as a positive WNPUI corresponds to easterly anomalies over the tropical WNP.

WNP and results in enhanced rainfall over the YRB (not shown). Therefore, to investigate the individual effect of tropical and extratropical circulation anomalies, it is necessary to eliminate their signals from each other.

To remove the signal of midlatitude circulation anomalies from tropical ones, we reselect the cases with the absolute values of WNPUI greater than 0.7 standard deviations and the absolute values of NEI smaller than 0.5 standard deviations (Fig. 4a), which can guarantee the total sum of NEI is near zero. Slightly modifying the criterion of NEI, for instance, smaller than 0.3 or 0.7 standard deviations, yields similar results. Similarly, cases with the absolute values of NEI greater than 0.7 standard deviations and that of the tropical westerly index smaller than 0.5 standard deviations (Fig. 4b) are used to eliminate the signal of tropical circulation anomalies from midlatitude ones. Here, the tropical westerly index is defined as the 850-hPa zonal wind anomalies averaged over 15°–25°N, 110°–130°E (Fig. 3b), which is slightly northward than that used to define WNPUI. This is because compared to WNPUI, the zonal wind anomalies over this region are more closely associated with NEI (Fig. 5), and thus the tropical anomalies can be removed more efficiently. There are 393 WNPUI+ cases, 385 WNPUI− cases, 318 NEI+ cases, and 309 NEI− cases left, respectively. In the following analyses, the anomalies associated with WNPUI and NEI refer to the composite difference between the newly selected WNPUI+ and WNPUI− cases and that between the newly selected NEI+ and NEI− cases, respectively.

Figure 6 shows the 850-hPa horizontal wind anomalies and rainfall anomalies associated with WNPUI and NEI after elimination. These anomalies resemble those before elimination (Fig. 3), except that there are no clear zonal wind anomalies

over the tropical WNP for NEI (Fig. 6b). The northeasterly anomalies averaged over 32.5°–40°N, 107.5°–120°E for WNPUI is −0.10 m s^{-1} and the tropical westerly anomalies averaged over 15°–25°N, 110°–130°E for NEI is 0.35 m s^{-1}, both of which are much weaker than those before elimination
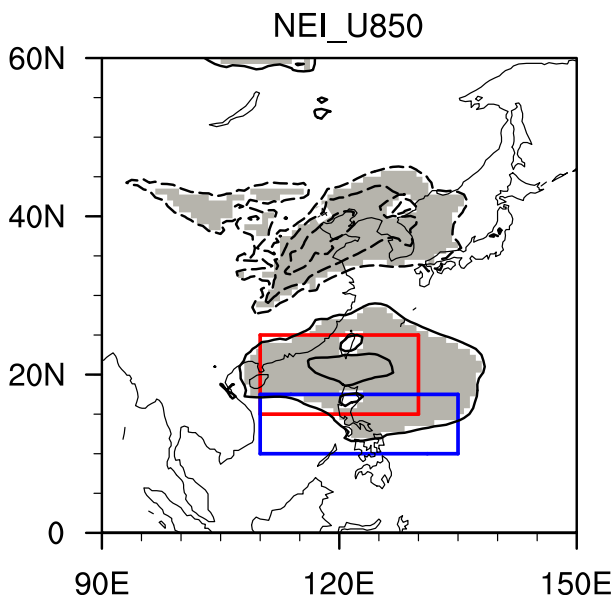

FIG. 5. As in Fig. 3b, but for the 850-hPa zonal wind anomalies. Shading indicates that the anomalies are significant at the 95% confidence level and greater than 2.0 m s^{-1}. The red box indicates the area used to define the tropical westerly index and the blue one to define the WNPUI.
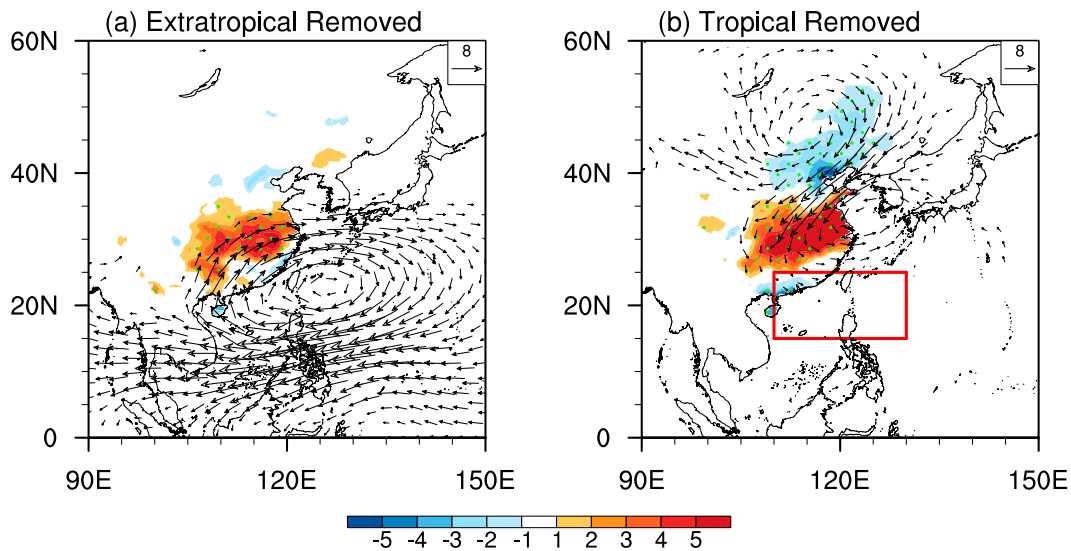
UV850 and Rainfall

FIG. 6. As in Fig. 3, but the extratropical and tropical signals have been removed, respectively (see text for details). The marked region in (b) indicates the area where the zonal wind anomalies in Fig. 3b are excluded.

(-0.99 and 1.93 m s^{-1}). These results suggest that the elimination process is effective. It should be noted that the YRB rainfall anomalies associated with NEI are much stronger than those associated with WNPUI. The YRBPI anomaly associated with NEI is 5.94 mm day^{-1}, greater than that associated with WNPUI (3.20 mm day^{-1}). These results suggest that NEI is more conducive to YRB rainfall than WNPUI.

We illustrate why the northeasterly anomalies can more efficiently induce the YRB rainfall than the tropical WNP anticyclonic anomaly from the perspective of equivalent potential temperature (θ_e). It has been well known that the summer YRB rainfall is characterized by a strong meridional gradient of humidity in the lower troposphere (Chen and Chang 1980;

Ding 1992) and thus θ_e, which combines moisture and temperature, has been widely used to describe the mei-yu rainfall (e.g., Zhu et al. 2007; Chen and Zhai 2015; Li and Lu 2017, 2018). A higher value of θ_e indicates a more humid and warmer condition. In climatological state, θ_e decreases with latitude over East Asia and shows its largest gradient over the YRB. An enhanced meridional gradient of θ_e over the YRB is favorable for frontogenesis and enhanced rainfall (Ninomiya 1984; Ninomiya and Shibagaki 2007).

Figure 7 shows the 850-hPa θ_e anomalies associated with WNPUI and NEI, respectively. To facilitate comparison, the significant rainfall and wind anomalies are also shown. The corresponding meridional gradient anomalies of θ_e, averaged over $107.5°–122.5°$E, are shown in the right-hand-side
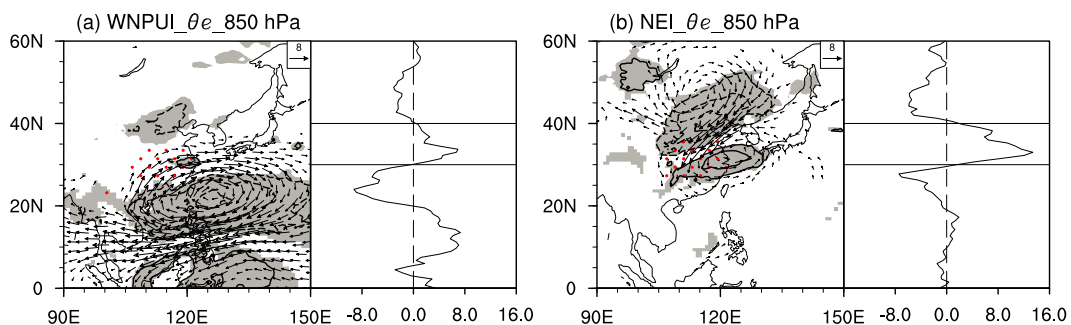

FIG. 7. Composite 850-hPa equivalent potential temperature (θ_e) anomalies (contours; K) associated with (a) WNPUI and (b) NEI. The contour interval is 0.2 K, and zero contours are omitted. Shading denotes the 95% confidence level. The significant positive rainfall anomalies (red stippling) and horizontal wind anomalies (vectors; m s^{-1}) at 850 hPa are also given for comparison. The curves in the right-hand-side plots show the corresponding meridional gradient anomalies (10^{-6} K km^{-1}) of θ_e, which are averaged over $107.5°–122.5°$E. Lower and upper horizontal lines indicate $30°$ and $40°$N, respectively.

subpanels. Here, a positive value represents the decrease in θ_e in the northward direction, i.e., the enhanced meridional gradient of θ_e. For WNPUI (Fig. 7a), there are positive θ_e anomalies over the YRB, corresponding to the southwesterly anomalies associated with the tropical WNP anticyclonic anomaly. These positive θ_e anomalies tend to enhance the meridional gradient of θ_e to the north of the YRB (right-hand-side subpanel of Fig. 7a). The intensified θ_e gradient favors enhanced rainfall over the YRB (Fig. 7a), but is located more northward (3°–5°) than rainfall anomalies. This is probably due to the northward tilt of the enhanced θ_e gradient with height in the lower troposphere (Li and Lu 2017). The difference between θ_e anomalies averaged over 30°N, 107.5°–122.5°E and those averaged over 40°N, 107.5°–122.5°E is 3.30 K, which is 27% of the climatological difference between these two edges in summer (12.45 K).

By contrast, for NEI (Fig. 7b), there are significant negative anomalies to the north of the YRB, which agree well with the northeasterly anomalies. Besides, positive θ_e anomalies appear over the YRB, in association with the southwesterly anomalies. These positive and negative θ_e anomalies strongly enhance the meridional gradient of θ_e over the YRB (right-hand-side subpanel of Fig. 7b). The enhanced θ_e gradient is in well agreement with the enhanced YRB rainfall and also locates slightly northward than rainfall anomalies. The difference between θ_e anomalies averaged over 30°N, 107.5°–122.5°E and those averaged over 40°N, 107.5°–122.5°E is 8.78 K, which is 71% of the climatological difference. As the enhanced θ_e gradient associated with NEI is much greater than that associated with WNPUI (Figs. 7a,b), NEI can more efficiently induce the YRB rainfall anomalies than WNPUI (Figs. 6a,b).

The results in this section indicate that the tropical WNP anticyclonic anomaly and the midlatitude northeasterly anomalies are both important for the YRB rainfall. Particularly, the heavier the YRB rainfall, the more requirement for the simultaneous occurrence of the tropical WNP anticyclonic anomaly and the midlatitude northeasterly anomalies. Moreover, the northeasterly anomalies can more efficiently enhance the YRB rainfall than the tropical anticyclonic anomaly. Therefore, it is necessary to explore whether there is any precursor signal for these tropical and extratropical circulation anomalies, especially for the extratropical circulation anomalies.

4. Evolutions of the tropical and extratropical circulation anomalies

a. Evolutions associated with heavy rainfall over the YRB

We shed light on the heavy rainfall days with YRBPI $\geq$ 15 mm day^{-1} (273 days). To ensure that the evolutions of anomalies associated with heavy YRB rainfall are nonoverlapping, heavy rainfall days with an interval of no more than 5 days are viewed as a heavy rainfall event and the first occurrence day is denoted as the reference (day 0). A total of 150 events are detected during the 42 boreal summers, which correspond to 3–4 events per year with a mean duration of 1–2 days.

Figure 8 shows the 850-hPa horizontal wind and rainfall anomalies from days −3 to +2 associated with the heavy rainfall events. The tropical WNP anticyclonic anomaly is stable from days −3 to +2 (Figs. 8a–f), and the southwesterly anomalies associated with the anticyclonic anomaly transport water vapor to East Asia, providing a favorable background for heavy rainfall. By contrast, the midlatitude northeasterly anomalies only appear from days −1 to +1 (Figs. 8c–e), implying a high-frequency variability of the extratropical circulation anomalies. Significant positive rainfall anomalies appear over the YRB at day −1 (Fig. 8c), peak at day 0 (Fig. 8d), and further sustain to day +1 (Fig. 8e), consistent with the evolution of the northeasterly anomalies. These results confirm that heavy rainfall requires the cooperation of the tropical anticyclonic anomaly and the midlatitude northeasterly anomalies.

Figure 9 displays the evolutions of the rainfall and circulation indices. The YRBPI starts to increase at day −1 and reaches its maximum at day 0 (Fig. 9a), with a value of 18.18 mm day^{-1}. Enhanced rainfall sustains to day +1 (12.74 mm day^{-1}), suggesting a mean duration of 1–2 days of the heavy rainfall. The variation of WNPUI is slow and positive values appear from days −6 to +6 (Fig. 9b). The evolution of NEI resembles that of YRBPI (Fig. 9c), i.e., northeasterly anomalies appear to the north of YRB at day −1, peak at day 0, and sustain to day +1. These results are all consistent with the spatial distribution (Fig. 8) and suggest that the dominant periods of the tropical and extratropical circulation anomalies are distinct. In addition, the WNPUI reaches its maximum at day −1 (Fig. 9b), which leads 1 day ahead of the YRB rainfall. This is because the southwesterly anomalies to the south of YRB lag the tropical easterly anomalies and become strongest at day 0 (not shown).

b. Evolutions associated with WNPUI and NEI

To investigate the composite temporal and spatial evolutions of the tropical and extratropical circulation anomalies, strong WNPUI and NEI days selected in section 3 with an interval of no more than 5 days are viewed as an event and day 0 refers to the first occurrence day of strong WNPUI and NEI. There are 157 WNPUI+, 138 WNPUI−, 223 NEI+, and 213 NEI− events obtained. The composite difference between WNPUI+ and WNPUI− events and that between the NEI+ and NEI− events are analyzed.

Figure 10 shows the 850-hPa horizontal wind and rainfall anomalies associated with the WNPUI events from days −4 to +6 and those associated with the NEI events from days −2 to +3. The evolution of WNPUI shows a biweekly feature (Figs. 10a–f). The anticyclonic anomaly has already appeared over the tropical WNP at day −4 (Fig. 10a). The anticyclonic anomaly gradually expands northwestward and southwesterly anomalies occupy south of the YRB at day 0 (Fig. 10c), which favor positive rainfall anomalies there. The southwesterly anomalies and positive rainfall anomalies further develop and reach their maximums at day +2 (Fig. 10d). These
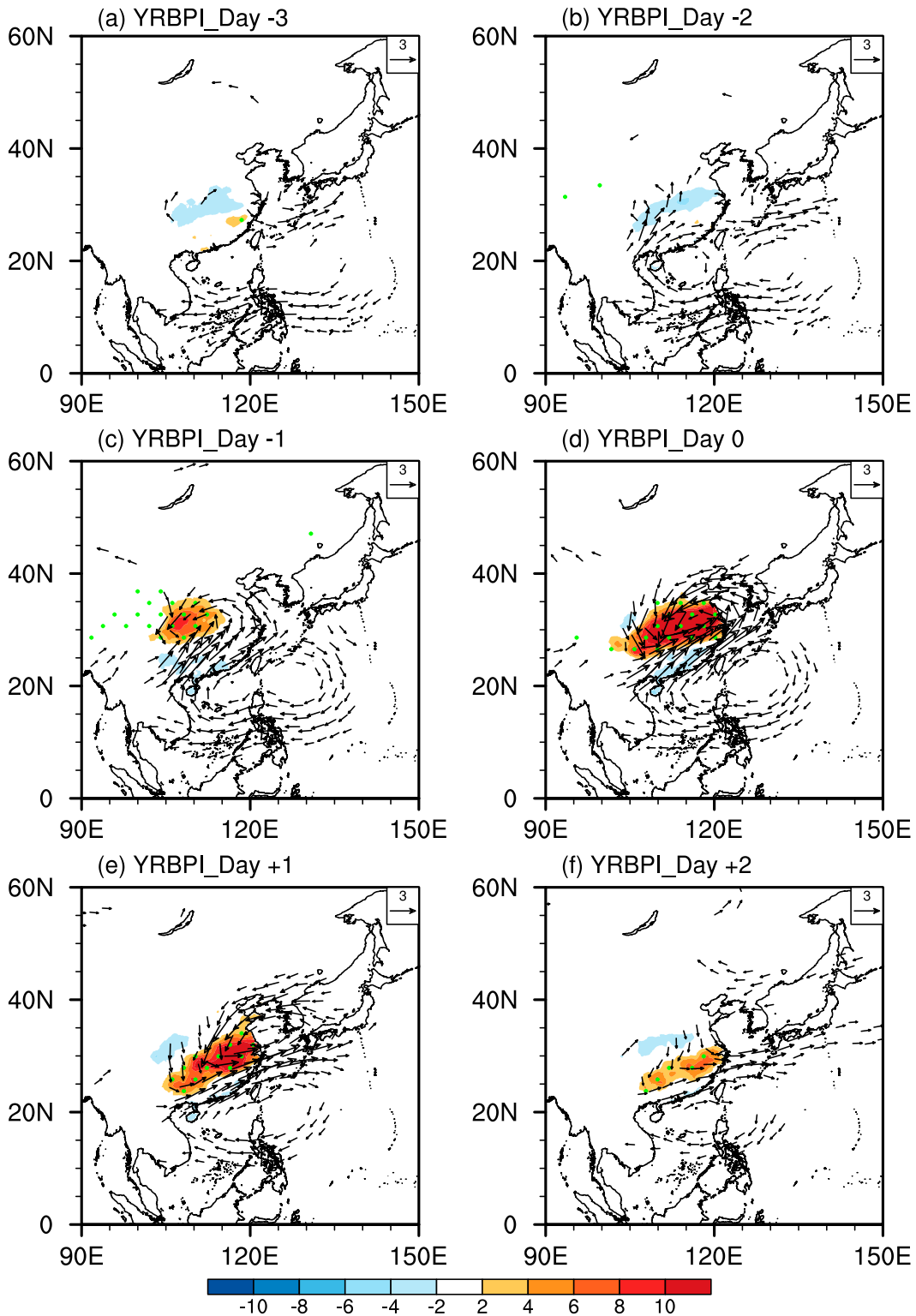
FIG. 8. Composite evolutions of the 850-hPa horizontal wind (vectors; m s^{-1}) and rainfall anomalies (shading; mm day^{-1}) from days -3 to $+2$ associated with heavy rainfall events over the YRB (YRBPI $\geq$ 15 mm day^{-1}). Shading significant at the 95% confidence level is stippled as green and vectors are shown only when they are significant in at least one direction.
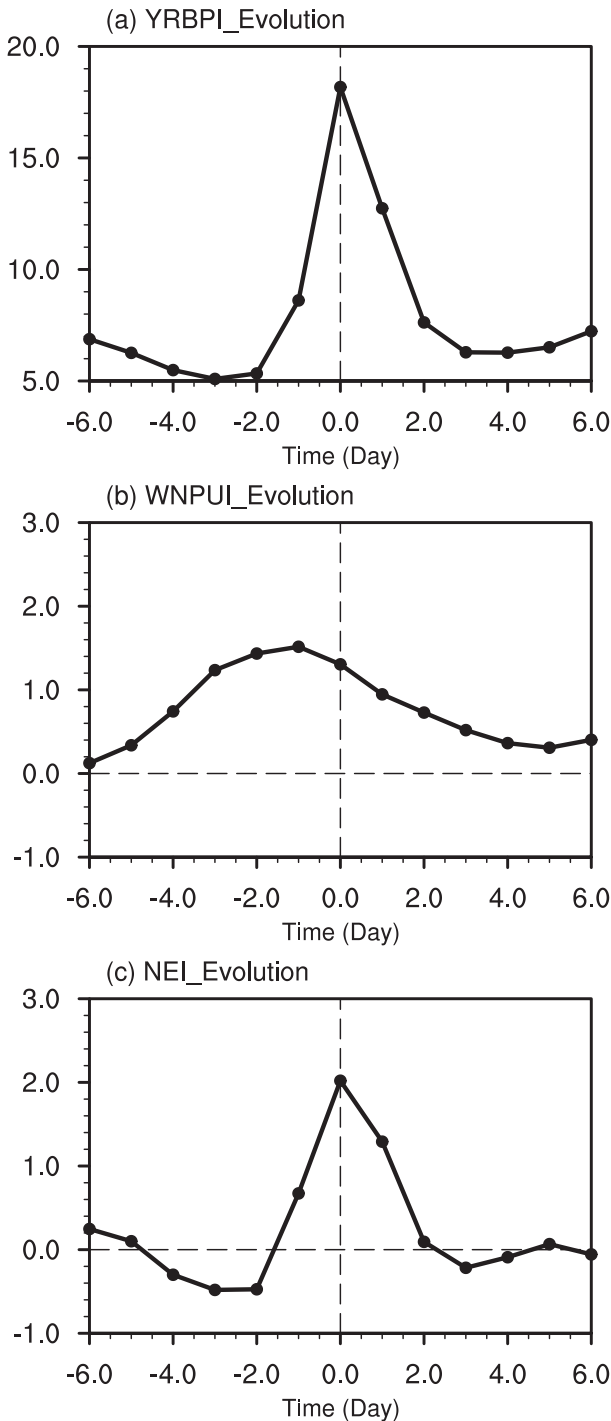
FIG. 9. Evolutions of (a) YRBPI (mm day^{-1}), (b) WNPUI (m s^{-1}), and (c) NEI (m s^{-1}) associated with heavy rainfall events over the YRB.

circulation and rainfall anomalies can be maintained to at least day +6 (Fig. 10f). Therefore, the tropical circulation anomalies provide a stable background for heavy rainfall over the YRB.

By contrast, the extratropical northeasterly anomalies and the associated YRB rainfall anomalies show synoptic features (Figs. 10g–l). An anticyclonic anomaly can be traced back to around the Lake Baikal at day −2 (Fig. 10g), with northerly and northeasterly anomalies over eastern Inner Mongolia. The anticyclonic anomaly and the associated northeasterly anomalies develop southeastward and reach their peaks at day 0 (Fig. 10i). Meanwhile, significant positive rainfall anomalies appear over the YRB and negative rainfall anomalies appear over North China and northeast China (Fig. 10i). In addition, a cyclonic anomaly appears over the YRB. This pair of anticyclonic anomaly and cyclonic anomaly and the associated positive rainfall anomalies over the YRB maintain until day +1 (Fig. 10j) and then decay fast (Figs. 10k,l).

The lead–lag results also suggest that the YRB rainfall anomalies associated with NEI are stronger than those associated with WNPUI. The maximum values of the YRBPI anomaly for NEI and WNPUI are 6.29 (at day 0) and 3.58 (at day +2) mm day^{-1}, respectively. These results confirm that the midlatitude northeasterly anomalies can more efficiently induce the YRB rainfall anomalies than the tropical anticyclonic anomaly. In addition, it should be noted that the northeasterly anomalies cannot be a response to the enhanced YRB rainfall, for instance, there is no clear northeasterly anomalies at days +2 or +4 of WNPUI (Figs. 10d,e), when there are strong and significant rainfall anomalies over the YRB.

Figure 11 shows the 200-hPa horizontal wind and meridional wind anomalies from days −10 to +4 associated with the NEI events. Here, the anomalies averaged over the two adjacent days are shown. At day 0 (Fig. 11d), there is a significant and strong anticyclonic anomaly around Lake Baikal, favoring its counterpart in the lower troposphere (Fig. 10i). There are two kinds of precursor signals that contribute to this anticyclonic anomaly (Fig. 11b): a cyclonic anomaly over midlatitude central Asia and an anticyclonic anomaly in the high latitudes over northwest of Lake Baikal. The former corresponds to the propagation of a zonally oriented teleconnection along the midlatitude Asian westerly jet. The meridional wind disturbances appear around the Mediterranean Sea at days −10 and −9 (Fig. 11a). These anomalies grow and propagate eastward, forming a wave train over the midlatitude Eurasia with a wavelength of around 60° (e.g., Fig. 11g). The action centers of the meridional wind anomalies appear over 30°, 60°, 90°, and 120°E, respectively (Fig. 11g), resembling the so-called Silk Road pattern in early summer (Hong et al. 2018). The fact that the midlatitude wave train plays a role in affecting the lower-tropospheric northeasterly anomalies agrees with some previous studies to a certain extent (e.g., Shang et al. 2020), which suggested that some extreme rainfall events over the YRB are affected by the midlatitude teleconnection.

On the other hand, the anticyclonic anomaly around Lake Baikal represents the contribution from high latitudes. The anticyclonic anomaly at days −2 and −1 (Fig. 11b) gradually moves southeastward and favors the lower-tropospheric anticyclonic anomaly together with the midlatitude wave train at day 0 (Fig. 11d). In addition, at day 0 (Fig. 11d), there is a
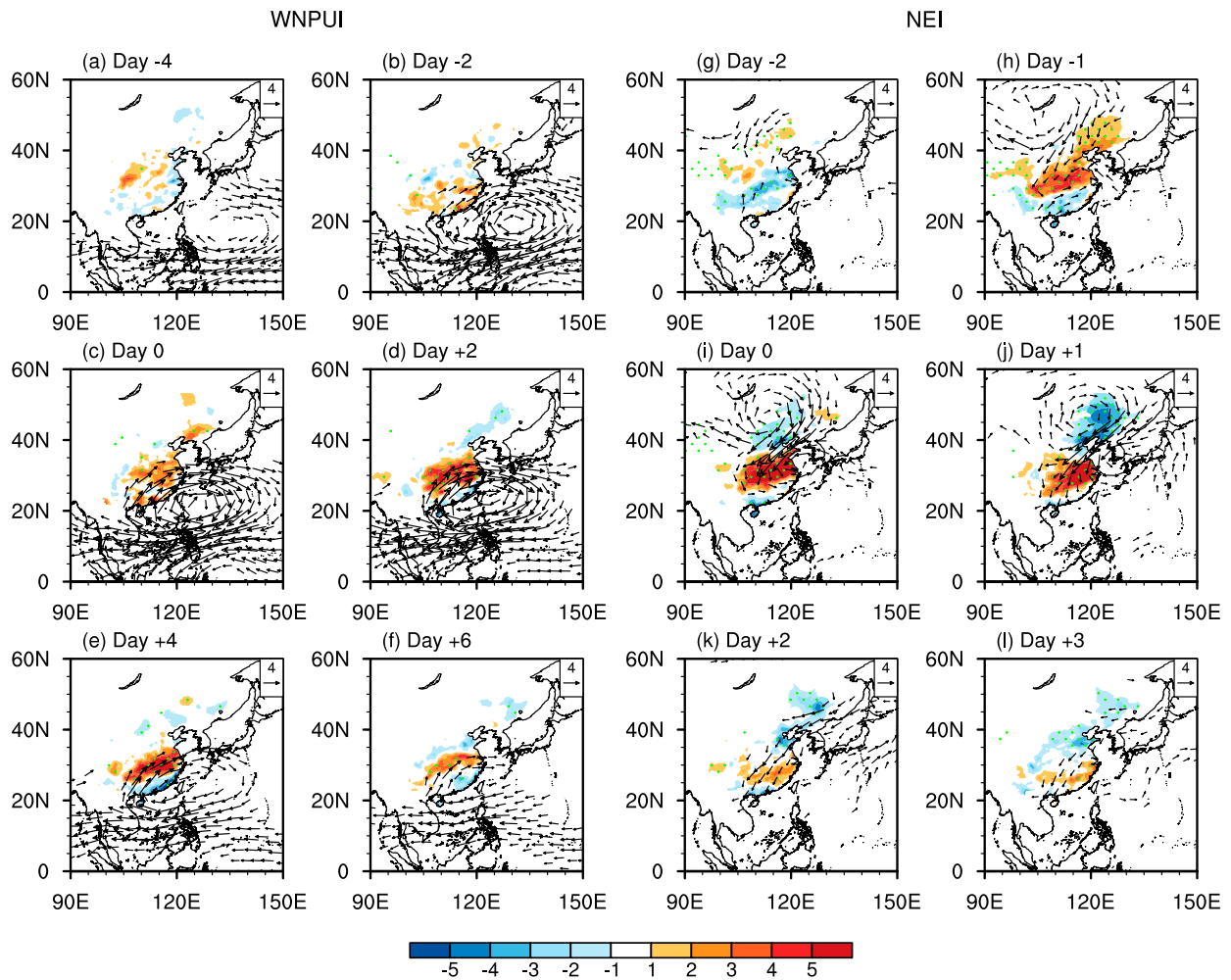
FIG. 10. Composite evolutions of the 850-hPa horizontal wind (vectors; m s^{-1}) and rainfall (shading; mm day^{-1}) anomalies from days −4 to +6 associated with (a)–(f) the WNPUI events and those from days −2 to +3 associated with (g)–(l) the NEI events. Shading significant at the 95% confidence level is stippled as green and vectors are shown only when they are significant in at least one direction.

cyclonic anomaly to the east of the anticyclonic anomaly, which corresponds to the lower-tropospheric cyclonic anomaly over the YRB (Fig. 10i). It is notable that the anticyclonic anomaly in the upper troposphere is located westward relative to its counterpart in the lower troposphere (Figs. 11d and 10i), suggesting a quasi-baroclinic feature of the anticyclonic anomaly. And the cyclonic anomaly in the upper troposphere is located poleward relative to its counterpart in the lower troposphere (Figs. 11d and 10i), suggesting a poleward tilt of the circulation anomalies. This northward tilt of circulation anomalies is a typical phenomenon over East Asia in summer (e.g., Yamazaki and Chen 1993) and may be related to more effectively gaining energy from the vertically sheared jets (Kosaka and Nakamura 2006).

To further address the origins of the cyclonic anomaly in midlatitude central Asia and the anticyclonic anomaly near the Lake Baikal, we define two vorticity indices. The midlatitude vorticity index (MVI) is defined as the 200-hPa vorticity

anomalies averaged over 32.5°–47.5°N, 65°–90°E. Therefore, a positive MVI indicates a cyclonic anomaly over midlatitude central Asia. The high-latitude vorticity index (HVI) is defined as the 200-hPa vorticity anomalies averaged over 50°–65°N, 85°–110°E, and then multiplied by −1 so that a positive HVI corresponds to an anticyclonic anomaly over northwest Lake Baikal and thus northeasterly anomalies to the north of YRB. Figure 12 shows the scatter diagram of standardized MVI and HVI. The cases in each quadrant are comparable. The cases in the four quadrants are 1606, 1782, 1567, and 1471, respectively. Therefore, these two indices tend to be independent of each other.

Similar to the WNPUI or NEI events, we also merge strong MVI or HVI (absolute values greater than 0.7 standard deviations) with an interval of no more than 3 days into an event. There are 184 MVI+, 186 MVI−, 260 HVI+, and 249 HVI− events obtained, respectively. The composite difference between MVI+ and MVI− events and that between the HVI+
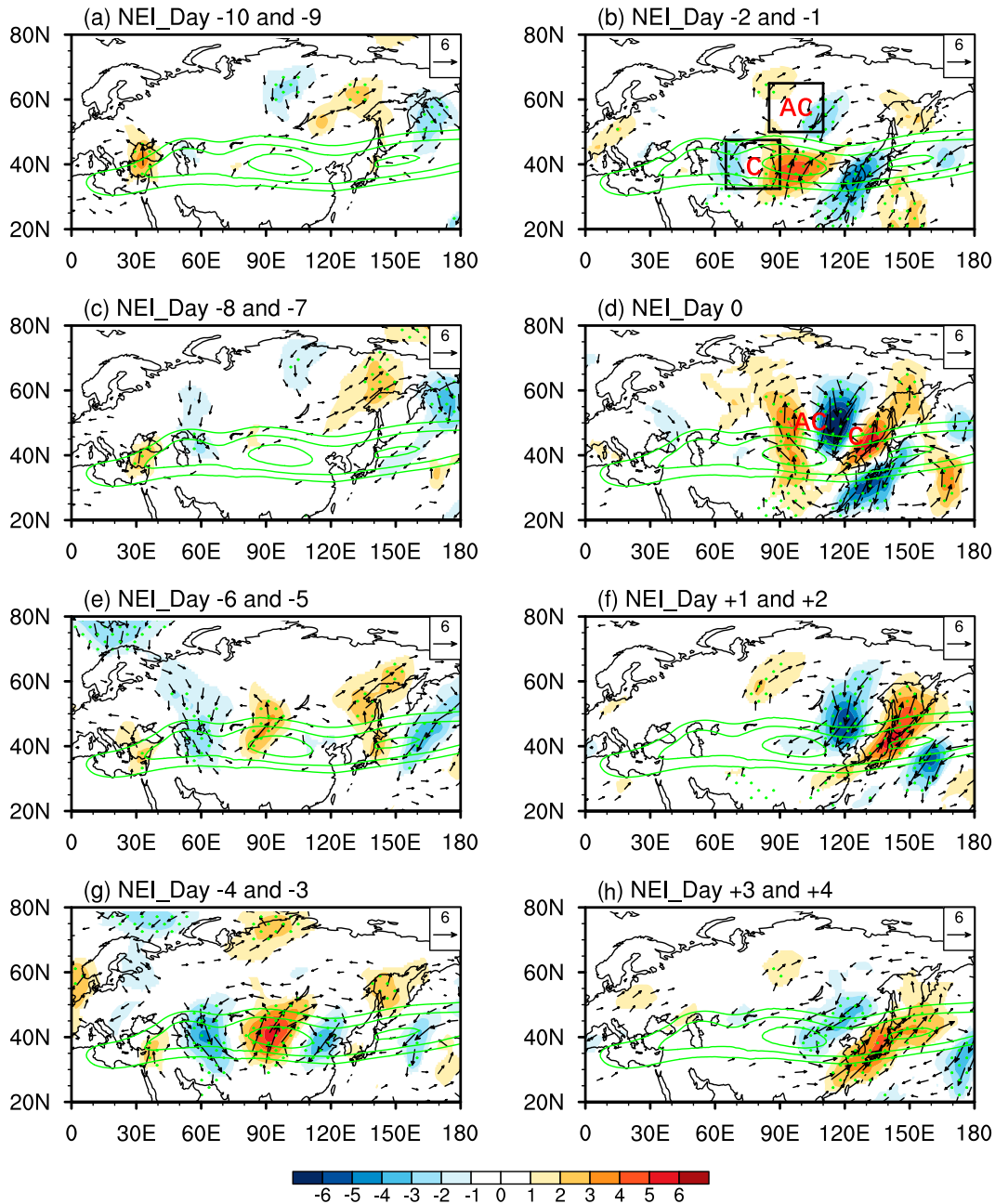
FIG. 11. Composite evolutions of the 200-hPa horizontal wind (vectors; m s^{-1}) and meridional wind (shading; m s^{-1}) anomalies from days −10 to +4 associated with the NEI events. Here, the anomalies are shown as the average of the adjacent two days, except for day 0. For instance, (a) is the average of days −10 and −9 and (c) is the average of days −8 and −7. Shading significant at the 95% confidence level is stippled as green and vectors are shown only when they are significant in at least one direction. The green contours represent the climatological zonal wind greater than 20.0 m s^{-1} in summer. "AC" and "C" represent anticyclonic and cyclonic anomalies, respectively. The marked regions in (b) are used to define the MVI and HVI, which are used for latter analysis.

and HVI− events are used to represent the anomalies associated with the MVI and HVI events, respectively.

Figure 13 shows the 200-hPa horizontal wind and meridional wind anomalies from days −3 to +4 associated with the MVI events. The upper-tropospheric circulation anomalies

are characterized by the evolution of a wave train along the midlatitude westerly jet. At around day −3, there are significant meridional wind disturbances in the entrance of the Asian westerly jet (Fig. 13a) and these disturbances propagate eastward with a wavelength of around 60° (e.g., Fig. 13g). The
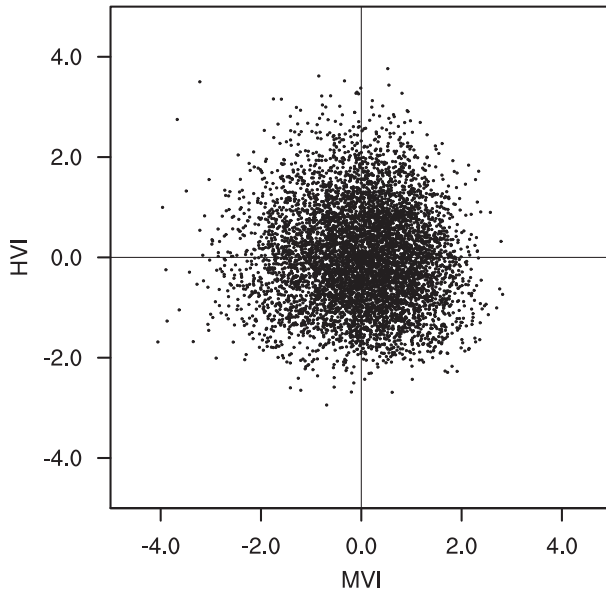
FIG. 12. Scatter diagram of the standardized MVI and HVI.

cyclonic anomaly over central Asia reaches its maximum day 0 (Fig. 13g) and the downstream anticyclonic anomaly over East Asia becomes strong at days +2 and +3 (Figs. 13d,f), favoring the lower-tropospheric northeasterly anomalies to the north of the YRB. These results confirm that the midlatitude wave train acts as one of the precursor signals of the lower-tropospheric northeasterly anomalies.

The 200-hPa circulation anomalies associated with the HVI events are characterized by a strong and significant anticyclonic anomaly over northwest of Lake Baikal at day 0 (Fig. 14g), which tends to be associated with the development of a well-organized wave train in the high-latitude Eurasia (left-hand-side panels of Fig. 14). The wave train propagates eastward from Europe to Lake Baikal and then southeastward to East Asia, with a wavelength of around 60°. Associated with the growth of the wave train, the anticyclonic anomaly appears at around 75°E at day −3 (Fig. 14a). It moves eastward and peaks at around 90°E at day 0 (Fig. 14g) and moves further downstream at day +1 (Fig. 14b), favoring its counterpart in the lower troposphere (Fig. 10i). These results suggest that the high-latitude wave train in the upper troposphere is crucial for the anticyclonic anomaly around Lake Baikal and the associated northeasterly anomalies in the lower troposphere. To our knowledge, the circulation anomalies associated with the anticyclonic anomaly have not been noted in the previous studies. The nature of this anticyclonic anomaly deserves further investigation.

The development and propagation of the wave trains can also be found at Fig. 15, which shows the evolutions of 200-hPa meridional wind anomalies averaged over 30°–50°N associated with the MVI events and those averaged over 45°–70°N associated with the HVI events, from days −6 to +6. For the MVI events (Fig. 15a), significant precursor signals can be traced back to day −3 at around 10°E. The wave energy gradually

propagates downward and at day 0, the northerly anomalies at 60°E and the southerly anomalies at 90°E reach their maximums, suggesting a cyclonic anomaly over the mid-latitude central Asia. The northerly anomalies at 120°E peak at day +2, favoring the lower-tropospheric northerly anomalies to the north of the YRB. For the HVI events (Fig. 15b), proceeding signals can be found at day −4, at around 30°E. The southerly anomalies at 75°E and northerly anomalies at 105°E peak at day 0, suggesting an anticyclonic anomaly there. This anticyclonic anomaly gradually moves downward and favors its counterpart in the lower troposphere, i.e., the anticyclonic anomaly over eastern Mongolia and Northeast China (Figs. 6b and 10i), at days +1 and +2. On the other hand, there is a cyclonic anomaly to the east of this anticyclonic anomaly at days +1 and +2, favoring the lower-tropospheric cyclonic anomaly over the YRB (Figs. 6b and 10i). These anomalies are consistent with the spatial evolutions of the 200-hPa circulation anomalies (Figs. 13 and 14). In addition, it is interesting to note that the wave train associated with HVI events keeps an eastward phase speed of about 5° day^{-1} throughout its life cycle (Fig. 15b), while the midlatitude wave train has a similar phase speed only in its developing stage and slows down in the latter stage (Fig. 15a).

5. Conclusions and discussion

The tropical and extratropical circulation anomalies both play an important role in affecting the YRB rainfall in summer. In this study, we investigate the characteristics of the tropical and extratropical circulation anomalies that directly affect the YRB rainfall. The tropical circulation anomalies manifest as an anticyclonic (cyclonic) anomaly over the tropical WNP and the extratropical circulation anomalies are characterized by a cyclonic (anticyclonic) anomaly over the YRB in the lower troposphere. Associated with the midlatitude cyclonic (anticyclonic) anomaly, there are northeasterly (southwesterly) anomalies to the north of the YRB.

It is found that the heavier the YRB rainfall, the more necessary the simultaneous occurrence of the tropical WNP anticyclonic anomaly and the midlatitude northeasterly anomalies. In particular, the northeasterly anomalies can enhance the YRB rainfall more efficiently than the tropical anticyclonic anomaly, as the northeasterly anomalies can more effectively increase the meridional gradient of θ_e over the YRB.

The tropical anticyclonic anomaly shows notable intraseasonal variability. It maintains biweekly and thus provides a stable background for the enhanced rainfall over the YRB. The evolution of the tropical anticyclonic anomaly is probably associated with the tropical intraseasonal oscillation, which propagates northward from the equator toward the East Asian summer monsoon regions, as previous studies indicated (e.g., Mao et al. 2010; Yang et al. 2010; Li et al. 2018).

By contrast, the midlatitude northeasterly anomalies are dominated by synoptic variability. However, we can find significant preceding signals for these northeasterly anomalies about one week in advance. These preceding signals manifest as the downward propagation of two wave trains in the upper
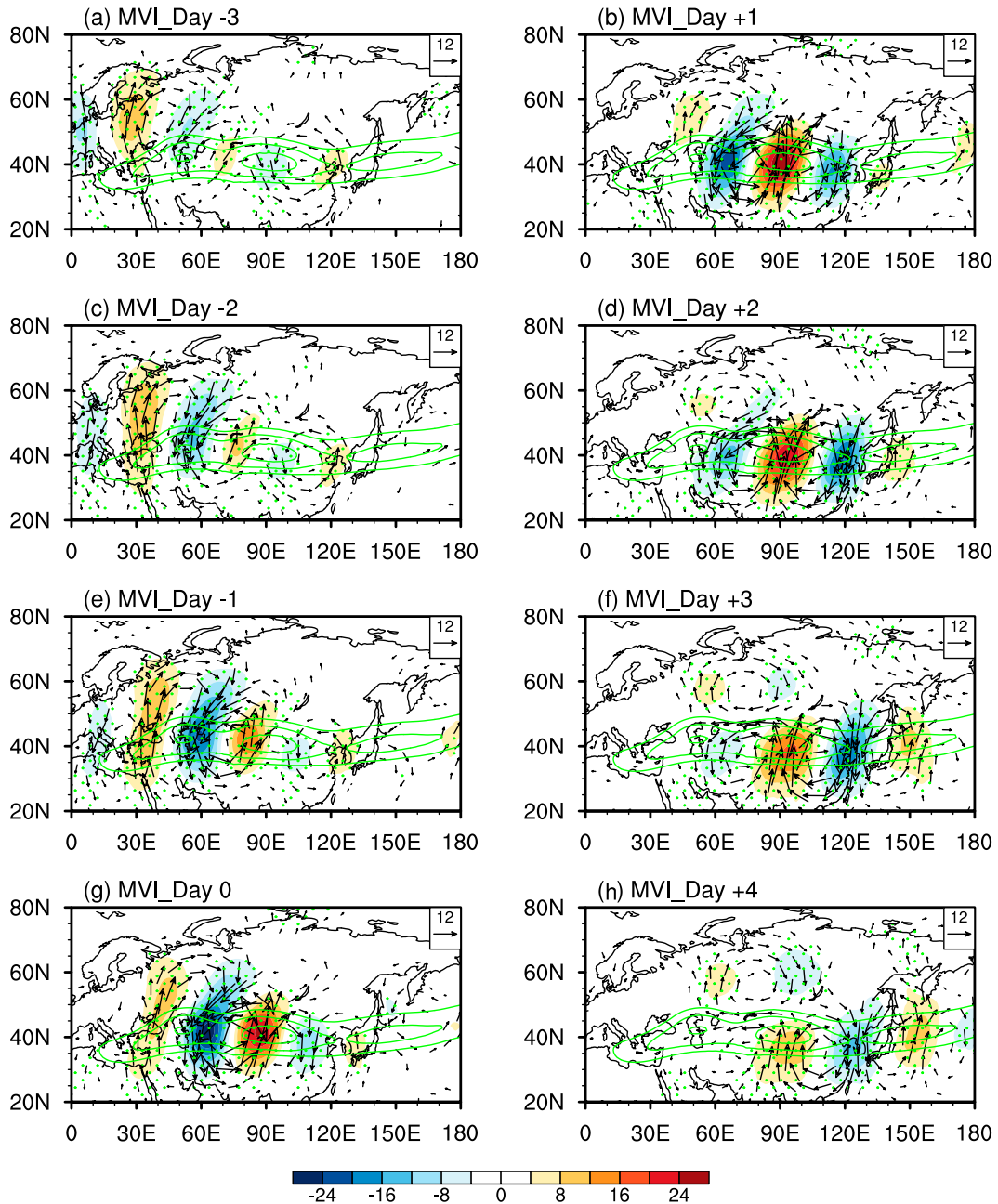
FIG. 13. Composite evolutions of the 200-hPa horizontal wind (vectors; m s^{-1}) and meridional wind (shading; m s^{-1}) anomalies from days -3 to $+4$ associated with the MVI events. Shading significant at the 95% confidence level is stippled as green and vectors are shown only when they are significant in at least one direction. The green contours represent the climatological zonal wind greater than 20.0 m s^{-1} in summer.

troposphere: a midlatitude one and a high-latitude one. The midlatitude wave train originates around the Mediterranean Sea and propagates eastward along the Asian westerly jet with a wavelength of about 60°. The other one propagates over the high-latitude Eurasian continent, from Europe eastward to Lake Baikal and then southeastward to East Asia, also with a wavelength of about 60°. These two wave trains tend to be independent of each other but both contribute to an anticyclonic anomaly over east of Inner Mongolia in the lower troposphere, favoring the development of the northeasterly anomalies to the north of the YRB. In addition, the high-latitude wave train also results in a cyclonic anomaly over the YRB in the lower troposphere, which also contributes to the northeasterly anomalies to the north of the YRB.
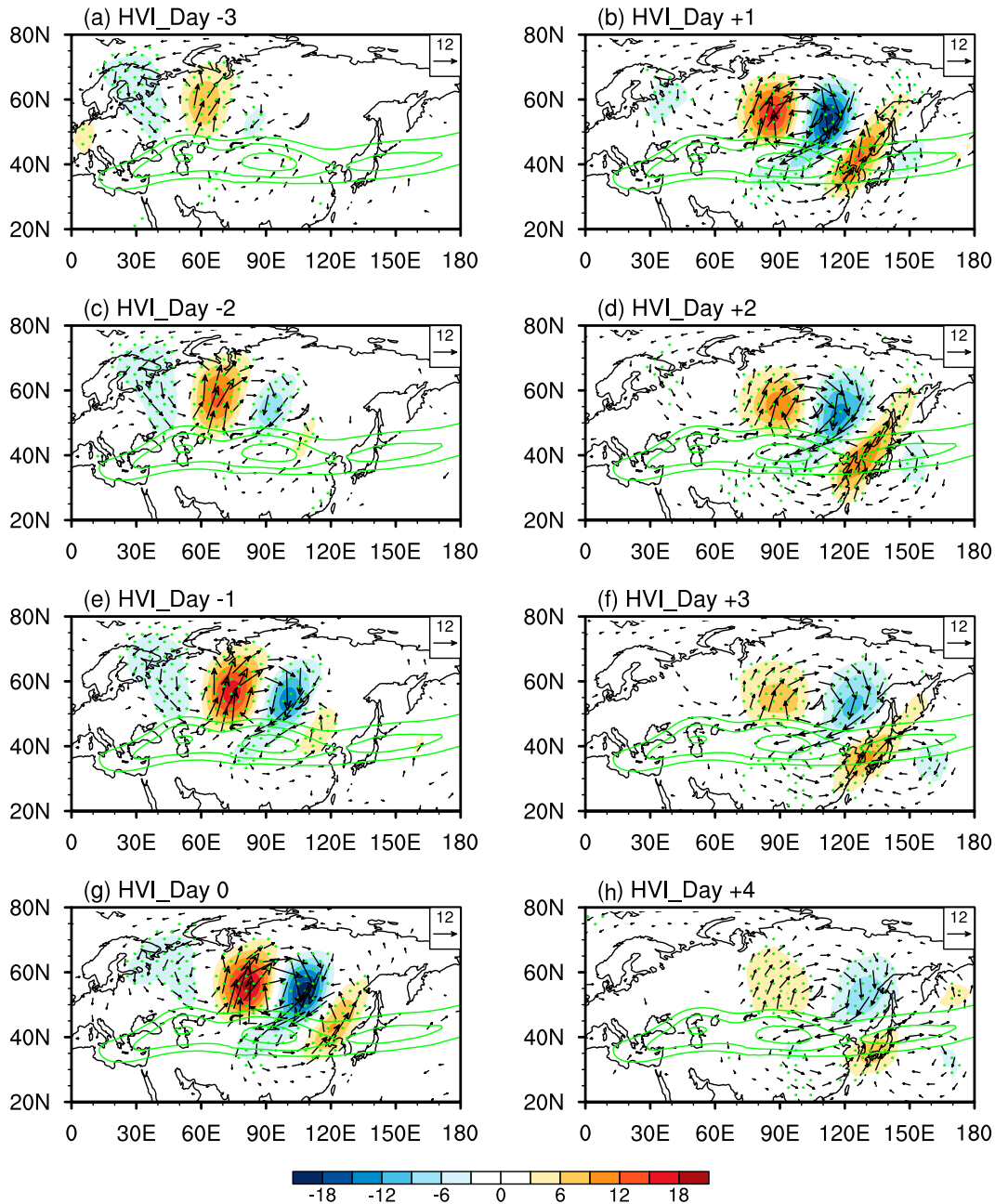
FIG. 14. As in Fig. 13, but for the HVI events.

It has been well known that the tropical WNP anticyclonic anomaly plays a key role in inducing heavy rainfall over the YRB. The results in this study indicate that compared to the tropical WNP anticyclonic anomaly, the midlatitude northeasterly anomalies can more efficiently enhance the YRB rainfall. Moreover, the heavier the YRB rainfall, the more requirement for the cooperation of the tropical and extratropical circulation anomalies. Therefore, to improve the forecast of heavy rainfall over the YRB, the circulation anomalies in the extratropics should be fully considered. Interestingly, there are significant precursor signals for these northeasterly anomalies, which provide a possibility for the forecast of extratropical anomalies. In addition, it seems that the northeasterly anomalies and the tropical WNP anticyclonic anomaly are negatively connected. The interaction between these tropical and extratropical circulation anomalies is an interesting topic for future study. Finally, it is necessary to investigate whether the tropical and extratropical circulation anomalies can be projected by climate models, which would be crucial for reliable projection of changes in
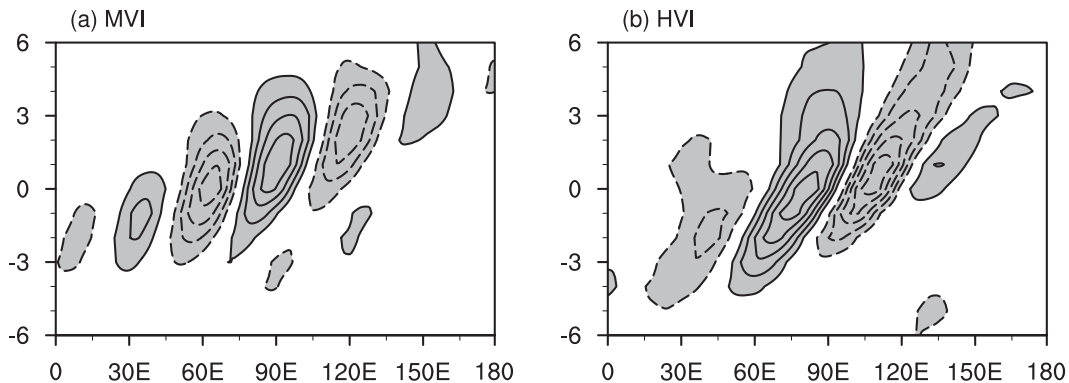
FIG. 15. Composite evolutions of the 200-hPa meridional wind anomalies (contours; m s^{-1}) (a) averaged over 30°–50°N associated with the MVI events and (b) those averaged over 45°–70°N associated with the HVI events, from days −6 to +6. The contour interval is 4.0 m s^{-1} in (a) and 2.0 m s^{-1} in (b) and zero contours are omitted. Shading indicates that the anomalies are significant at the 95% confidence level and greater than 4.0 m s^{-1} in (a) and 2.0 m s^{-1} in (b).

rainfall, particularly extreme rainfall, over the YRB in the future.

REFERENCES

Chang, C.-P., Y. Zhang, and T. Li, 2000: Interannual and interdecadal variations of the East Asian summer monsoon and tropical Pacific SSTs. Part I: Roles of the subtropical ridge. *J. Climate*, **13**, 4310–4325, https://doi.org/10.1175/1520-0442(2000)013<4310:IAIVOT>2.0.CO;2.

Chen, J., Z. Wen, R. Wu, Z. Chen, and P. Zhao, 2015: Influences of northward propagating 25–90-day and quasi-biweekly oscillations on eastern China summer rainfall. *Climate Dyn.*, **45**, 105–124, https://doi.org/10.1007/s00382-014-2334-y.

Chen, T.-J. G., and C.-P. Chang, 1980: The structure and vorticity budget of an early summer monsoon through (mei-yu) over southeastern China and Japan. *Mon. Wea. Rev.*, **108**, 942–953, https://doi.org/10.1175/1520-0493(1980)108<0942:TSAVBO>2.0.CO;2.

Chen, Y., and P. Zhai, 2015: Synoptic-scale precursors of the East Asia/Pacific teleconnection pattern responsible for persistent extreme precipitation in the Yangtze River Valley. *Quart. J. Roy. Meteor. Soc.*, **141**, 1389–1403, https://doi.org/10.1002/qj.2448.

Cheng, Y., L. Wang, and T. Li, 2021: Two distinct types of 10–30-day persistent heavy rainfall events over the Yangtze River Valley. *J. Climate*, **34**, 9571–9584, https://doi.org/10.1175/JCLI-D-20-0741.1.

Ding, H., R. J. Greatbatch, W. Park, M. Latif, V. Semenov, and X. Sun, 2014: The variability of the East Asian summer monsoon and its relationship to ENSO in a partially coupled climate model. *Climate Dyn.*, **42**, 367–379, https://doi.org/10.1007/s00382-012-1642-3.

——, ——, J. Lu, and B. Cash, 2015: The East Asian summer monsoon in pacemaker experiments driven by ENSO. *Ocean Dyn.*, **65**, 385–393, https://doi.org/10.1007/s10236-014-0795-5.

Ding, Y., 1992: Summer monsoon rainfalls in China. *J. Meteor. Soc. Japan*, **70**, 373–396, https://doi.org/10.2151/jmsj1965.70.1B_373.

——, 2005: *Advanced Synoptic Meteorology* (in Chinese). 2nd ed. China Meteorological Press, 585 pp.

——, Y. Liu, and Z.-Z. Hu, 2021: The record-breaking meiyu in 2020 and associated atmospheric circulation and tropical SST anomalies. *Adv. Atmos. Sci.*, **38**, 1980–1993, https://doi.org/10.1007/s00376-021-0361-2.

He, J., Z. Wu, Z. Jiang, C. Miao, and G. Han, 2007: "Climate effects" of the northeast cold vortex and its influence on meiyu. *Chin. Sci. Bull.*, **52**, 671–679, https://doi.org/10.1007/s11434-007-0053-z.

Hersbach, H., and Coauthors, 2020: The ERA5 global reanalysis. *Quart. J. Roy. Meteor. Soc.*, **146**, 1999–2049, https://doi.org/10.1002/qj.3803.

Hong, X., R. Lu, and S. Li, 2018: Differences in the Silk Road pattern and its relationship to the North Atlantic Oscillation between early and late summers. *J. Climate*, **31**, 9283–9292, https://doi.org/10.1175/JCLI-D-18-0283.1.

Hsu, H.-H., and C.-H. Weng, 2001: Northwestward propagation of the intraseasonal oscillation in the western North Pacific during the boreal summer: Structure and mechanism. *J. Climate*, **14**, 3834–3850, https://doi.org/10.1175/1520-0442(2001)014<3834:NPOTIO>2.0.CO;2.

Hu, K., R. Lu, and D. Wang, 2011: Cold vortex over northeast China and its climate effect (in Chinese). *Chin. J. Atmos. Sci.*, **35**, 179–191, https://doi.org/10.3878/j.issn.1006-9895.2011.01.15.

Hu, Y., Y. Deng, Z. Zhou, C. Cui, and X. Dong, 2019: A statistical and dynamical characterization of large-scale circulation patterns associated with summer extreme precipitation over the middle reaches of the Yangtze River. *Climate Dyn.*, **52**, 6213–6228, https://doi.org/10.1007/s00382-018-4501-z.

Huang, R., and F. Sun, 1992: Impacts of the tropical western Pacific on the East Asia summer monsoon. *J. Meteor. Soc. Japan*, **70**, 243–256, https://doi.org/10.2151/jmsj1965.70.1B_243.

Jia, X., and S. Yang, 2013: Impact of the quasi-biweekly oscillation over the western North Pacific on East Asian subtropical monsoon during early summer. *J. Geophys. Res. Atmos.*, **118**, 4421–4434, https://doi.org/10.1002/jgrd.50422.

Kosaka, Y., and H. Nakamura, 2006: Structure and dynamics of the summertime Pacific–Japan teleconnection pattern. *Quart. J. Roy. Meteor. Soc.*, **132**, 2009–2030, https://doi.org/10.1256/qj.05.204.

Li, D., Z. Li, Y. Zhou, and X. Lu, 2020: Substantial increases in the water and sediment fluxes in the headwater region of the Tibetan Plateau in response to global warming. *Geophys. Res. Lett.*, **47**, e2020GL087745, https://doi.org/10.1029/2020GL087745.

Li, J., J. Mao, and G. Wu, 2015: A case study of the impact of boreal summer intraseasonal oscillations on Yangtze rainfall. *Climate Dyn.*, **44**, 2683–2702, https://doi.org/10.1007/s00382-014-2425-9.

Li, X., and R. Lu, 2017: Extratropical factors affecting the variability in summer precipitation over the Yangtze River basin, China. *J. Climate*, **30**, 8357–8374, https://doi.org/10.1175/JCLI-D-16-0282.1.

——, and ——, 2018: Subseasonal change in the seesaw pattern of precipitation between the Yangtze River basin and the tropical western North Pacific during summer. *Adv. Atmos. Sci.*, **35**, 1231–1242, https://doi.org/10.1007/s00376-018-7304-6.

——, and ——, 2021: Decadal change in the influence of the western North Pacific subtropical high on summer rainfall over the Yangtze River basin in the late 1970s. *Adv. Atmos. Sci.*, **38**, 1823–1834, https://doi.org/10.1007/s00376-021-1051-9.

——, G. Gollan, R. J. Greatbatch, and R. Lu, 2018: Intraseasonal variation of the East Asian summer monsoon associated with the Madden-Julian Oscillation. *Atmos. Sci. Lett.*, **19**, e794, https://doi.org/10.1002/asl.794.

——, R. Lu, and G. Li, 2021: Different configurations of interannual variability of the western North Pacific subtropical high and East Asian westerly jet in summer. *Adv. Atmos. Sci.*, **38**, 931–942, https://doi.org/10.1007/s00376-021-0339-0.

Liang, X.-Z., and W.-C. Wang, 1998: Associations between China monsoon rainfall and tropospheric jets. *Quart. J. Roy. Meteor. Soc.*, **124**, 2597–2623, https://doi.org/10.1002/qj.49712455204.

Liu, H., D.-L. Zhang, and B. Wang, 2008: Daily to submonthly weather and climate characteristics of the summer 1998 extreme rainfall over the Yangtze River basin. *J. Geophys. Res.*, **113**, D22101, https://doi.org/10.1029/2008JD010072.

Liu, H.-B., Y. Yang, D.-L. Zhang, and B. Wang, 2014: Roles of synoptic to quasi-biweekly disturbances in generating the summer 2003 heavy rainfall in East China. *Mon. Wea. Rev.*, **142**, 886–904, https://doi.org/10.1175/MWR-D-13-00055.1.

Lu, R., 2000: Anomalies in the tropics associated with the heavy rainfall in East Asia during the summer of 1998. *Adv. Atmos. Sci.*, **17**, 205–220, https://doi.org/10.1007/s00376-000-0004-y.

——, and B. Dong, 2001: Westward extension of North Pacific subtropical high in summer. *J. Meteor. Soc. Japan*, **79**, 1229–1241, https://doi.org/10.2151/jmsj.79.1229.

Mao, J., Z. Sun, and G. Wu, 2010: 20–50-day oscillation of summer Yangtze rainfall in response to intraseasonal variations in the subtropical high over the western North Pacific and South China Sea. *Climate Dyn.*, **34**, 747–761, https://doi.org/10.1007/s00382-009-0628-2.

Ninomiya, K., 1984: Characteristics of baiu front as a predominant subtropical front in the summer Northern Hemisphere. *J. Meteor. Soc. Japan*, **62**, 880–894, https://doi.org/10.2151/jmsj1965.62.6_880.

——, and Y. Shibagaki, 2007: Multi-scale features of the meiyu-baiu front and associated precipitation systems. *J. Meteor. Soc. Japan*, **85B**, 103–122, https://doi.org/10.2151/jmsj.85B.103.

Park, J.-Y., J.-G. Jhun, S.-Y. Yim, and W.-M. Kim, 2010: Decadal changes in two types of the western North Pacific subtropical high in boreal summer associated with Asian summer monsoon/El Niño–Southern Oscillation connections. *J. Geophys. Res.*, **115**, D21129, https://doi.org/10.1029/2009JD013642.

Plate, E. J., 2002: Flood risk and flood management. *J. Hydrol.*, **267**, 2–11, https://doi.org/10.1016/S0022-1694(02)00135-X.

Ren, X., X.-Q. Yang, and X. Sun, 2013: Zonal oscillation of western Pacific subtropical high and subseasonal SST variations during Yangtze persistent heavy rainfall events. *J. Climate*, **26**, 8929–8946, https://doi.org/10.1175/JCLI-D-12-00861.1.

Sampe, T., and S.-P. Xie, 2010: Large-scale dynamics of the meiyu-baiu rainband: Environmental forcing by the westerly jet. *J. Climate*, **23**, 113–134, https://doi.org/10.1175/2009JCLI3128.1.

Shang, W., S. Li, X. Ren, and K. Duan, 2020: Event-based extreme precipitation in central-eastern China: Large-scale anomalies and teleconnections. *Climate Dyn.*, **54**, 2347–2360, https://doi.org/10.1007/s00382-019-05116-1.

Tao, S., and L. Chen, 1987: A review of recent research on the East Asian summer monsoon in China. *Monsoon Meteorology*, C.-P. Chang and T. N. Krishnamurti, Eds., Oxford University Press, 60–92.

Wang, S., H. Zuo, Y. Yin, J. Wang, and X. Ma, 2019: Asymmetric impact of East Asian jet's variation on midsummer rainfall in North China and Yangtze River Valley. *Climate Dyn.*, **53**, 6199–6213, https://doi.org/10.1007/s00382-019-04923-w.

Wilks, D. S., 2006: Hypothesis testing. *Statistical Methods in the Atmospheric Sciences*, International Geophysics Series, Vol. 91, Academic Press, 131–177.

Wu, J., and X. Gao, 2013: A gridded daily observation dataset over China region and comparison with the other datasets (in Chinese). *Chin. J. Geophys.*, **56**, 1102–1111, https://doi.org/10.6038/cjg20130406.

Xie, S.-P., Y. Kosaka, Y. Du, K. Hu, J. S. Chowdary, and G. Huang, 2016: Indo-western Pacific Ocean capacitor and coherent climate anomalies in post-ENSO summer: A review. *Adv. Atmos. Sci.*, **33**, 411–432, https://doi.org/10.1007/s00376-015-5192-6.

Xu, S., and L. Qi, 2023: Critical influence of the northeast cold vortex in different positions on precipitation. *Climate Dyn.*, **60**, 867–881, https://doi.org/10.1007/s00382-022-06365-3.

Yamazaki, N., and T.-C. Chen, 1993: Analysis of the East Asian monsoon during early summer of 1979: Structure of the baiu front and its relationship to large-scale fields. *J. Meteor. Soc. Japan*, **71**, 339–355, https://doi.org/10.2151/jmsj1965.71.3_339.

Yang, J., Q. Liu, and Z. Liu, 2010: Linking observations of the Asian monsoon to the Indian Ocean SST: Possible roles of Indian Ocean basin mode and dipole mode. *J. Climate*, **23**, 5889–5902, https://doi.org/10.1175/2010JCLI2962.1.

Yu, F., Z. Chen, X. Ren, and G. Yang, 2009: Analysis of historical floods on the Yangtze River, China: Characteristics and

explanations. *Geomorphology*, **113**, 210–216, https://doi.org/10.1016/j.geomorph.2009.03.008.

Zhou, T.-J., and R.-C. Yu, 2005: Atmospheric water vapor transport associated with typical anomalous summer rainfall patterns in China. *J. Geophys. Res.*, **110**, D08104, https://doi.org/10.1029/2004JD005413.

Zhu, Q. G., J. R. Lin, S. W. Shou, and D. S. Tang, 2007: *Principles and Methods of Synoptic Meteorology* (in Chinese). China Meteorological Press, 267 pp.

Zwiers, F. W., and H. von Storch, 1995: Taking serial correlation into account in tests of the mean. *J. Climate*, **8**, 336–351, https://doi.org/10.1175/1520-0442(1995)008<0336:TSCIAI>2.0.CO;2.